Title

Direct Surface Tension Measurements of Individual Sub-Micrometer Particles Using Atomic Force Microscopy

Journal

The Journal of Physical Chemistry A, 121(43)

ISSN

1089-5639

Authors

Lee, Hansol D
Estillore, Armando D
Morris, Holly S
et al.

Publication Date

2017-11-02

DOI

10.1021/acs.jpca.7b04041

Peer reviewed

THE JOURNAL OF PHYSICAL CHEMISTRY A

Article

Cite This: J. Phys. Chem. A XXXX, XXX, XXX-XXX

pubs.acs.org/JPCA

Direct Surface Tension Measurements of Individual Sub-Micrometer Particles Using Atomic Force Microscopy

Published as part of The Journal of Physical Chemistry virtual special issue "Veronica Vaida Festschrift".

Hansol D. Lee,[†] Armando D. Estillore,[‡,#] Holly S. Morris,[†] Kamal K. Ray,[†] Aldair Alejandro,[†] Vicki H. Grassian,[*,‡,§] and Alexei V. Tivanski[*,†]

[†]Department of Chemistry, University of Iowa, Iowa City, Iowa 52242, United States

[‡]Department of Chemistry and Biochemistry and [§]Department of Nanoengineering and Scripps Institute of Oceanography, University of California, San Diego, La Jolla, California 92093, United States

Supporting Information

ABSTRACT: Understanding the role of sea spray aerosol (SSA) on climate and the environment is of great interest due to their high number concentration throughout the Earth's atmosphere. Despite being of fundamental importance, *direct* surface tension measurements of SSA relevant sub-micrometer particles are rare, largely due to their extremely small volumes. Herein, atomic force microscopy (AFM) is used to directly measure the surface tension of individual sub-micrometer SSA particle mimics at ambient temperature and varying relative humidity (RH). Specifically, we probed both atmospherically relevant and fundamentally important model systems including electrolyte salts, dicarboxylic acids, and saccharides as single components and mixtures. Our results show that the single particle surface tension depends on RH or solute mole percentage and chemical composition. Moreover, for liquid droplets at and below 100 Pa s in viscosity, or at corresponding RH, we show good agreement between the AFM single particle and the bulk solution surface tension measurements at overlapping concentration ranges. Thus, direct surface tension measurements of individual particles using AFM is shown over a wide range of chemical systems as a function of RH, solute mole percentage, and viscosity than previously reported.

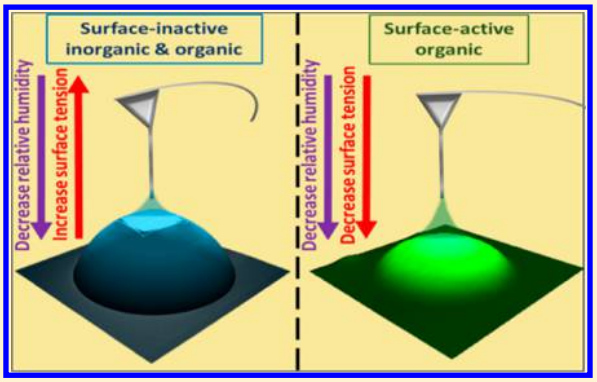

INTRODUCTION

Modeling chemical processes of the atmosphere and climate remains a challenge, due to the complexity of the Earth's atmosphere with a large number of contributing factors from anthropogenic and natural sources.[1−5] In particular, major focus has been toward better understanding the impact of atmospheric aerosols. It has been shown that sea spray aerosol (SSA) particles in the submicron size range generated from breaking waves can both directly and indirectly reflect solar radiation.[6−9] Direct aerosol effects are attributed to scattering and absorption of solar radiation, while indirect effects refer to the ability of aerosols to act as cloud condensation nuclei and therefore facilitate cloud formation. Still, accurate predictions of the combined role of the SSA effects remain a challenge.

Currently, few models attempt to reconcile this gap in our understanding. κ-Köhler theory is frequently used to predict the effect of SSA on cloud formation, where the cloud activation can be predicted using a dimensionless hygroscopicity parameter, κ, and assuming surface tension of a liquid droplet is fixed value equal to that of pure water.[10] More recently, the compressed film model was established to predict cloud activation using a two-dimensional equation of state that accounts for the surface activity of organic species behaving as surfactants packing the liquid−gas interface.[11,12] A key factor in both of these models is the surface tension of the aerosol, as it plays a critical role in predicting cloud activation. Moreover, the assumption that surface tension is a simple constant equal to that of pure water may lead to erroneous predictions of the hygroscopicity parameter κ, in particular, if surfactants can efficiently suppress overall surface tension of a droplet.[11−13] Therefore, measurements of surface tension of particles as a function of relative humidity (RH) are needed to establish relevant constraints on the surface tension of nascent atmospheric droplets.

To address this problem, there are few examples of measurements combined with empirical modeling of surface tension of single particles. The optical tweezers method was used to isolate single particles on the order of 10−20 μm in diameter, to *indirectly* quantify surface tension as a function of RH.[14] The approach can be highly advantageous, since the

Received: April 28, 2017
Revised: September 21, 2017
Published: October 5, 2017

DOI: 10.1021/acs.jpca.7b04041
J. Phys. Chem. A XXXX, XXX, XXX−XXX

experimental method is contact-free and droplets are in a suspended state. However, surface tension studies limited in this supermicron size regime do not necessarily correspond to the population of submicron-ranged particles that are abundant in SSA. Smaller particles generally have longer lifetimes in the atmosphere, contain larger concentrations of organic matter, and display size-dependent properties.[15−19] Thus, we recently developed the methodology to use atomic force microscope (AFM) as a means to probe surface tension of substrate-deposited particles. With a constant radius nanoneedle, the surface tension of sub-micrometer single particles can be *directly* and quantitatively measured as a function of RH.[20]

In this study, we extend the chemical systems that cover a wide range of viscosities and RH range to improve our understanding of surface tension of SSA-relevant particles that contain both single- and multicomponent systems, chosen due to relevance to the atmosphere and importance as fundamental model systems.[21] By extending the experimental range of surface tension measurements, these data provide significant insight toward the development of accurate models by providing much-needed direct surface tension measurements of various chemical systems, but on a single particle basis.[22] To further validate our methodology, we made comparisons of single particle surface tension versus RH to bulk surface tension versus solute mole percentage, by also using a force tensiometer to perform bulk solution surface tension measurements of the same chemical system. The comparison was made by using the water uptake data measured by a hygroscopic tandem differential mobility analyzer (HTDMA), which subsequently allows for direct comparison of these surface tension data. This comparison of bulk and single particle surface tension measurements is shown to be excellent at and below 1×10^2 Pa s in viscosity or, for most droplets, at and above 80% RH. Interestingly, when single particle surface tension of surface active compounds is measured above the saturation point to supersaturated concentration values, we observe lower values of surface tension relative to bulk that were not reported previously. We propose that this deviation is likely due to the surface activity that leads to formation of a closely packed molecular film at the air−liquid interface on the nanoneedle, similar to the compressed film model reported previously.[11,12]

EXPERIMENTAL METHODS

Substrate Deposited Particles. Aerosols were generated with a constant output atomizer (TSI, Inc., model 3076) from 1 mM aqueous solutions. All chemicals were purchased from Sigma-Aldrich, where NaCl, NaBr, malonic acid, glutaric acid, maleic acid, glucose, sucrose, and maltose were all reagent grade, 99.99% purity. All chemicals were used without additional purification and dissolved in deionized water (18 MΩ·cm). The aerosols were passed through a diffusion dryer (TSI, Inc., model 3062), and then particles were deposited by impaction onto a hydrophobically coated silicon wafer generated with polydimethylsiloxanes on the surface.[23] The silicon wafer was cleaned with ethanol and air-dried prior to use. Stage 6 of the micro orifice uniform deposit impactor (MOUDI; MSP, Inc., model 110) was used and has aerodynamic diameter range of 0.56−1 μm. The substrate deposited particles were prepared and studied on the same day.

Hygroscopic Tandem Differential Mobility Analyzer. The HTDMA hygroscopicity measurements as a function of RH at ambient temperature were performed using a multi-analysis aerosol reactor system (MAARS) that has been described previously in detail.[24] Briefly, dehydrated aerosol particles, less than 10% RH, were size-selected at 100 nm with a differential mobility analyzer (DMA1; TSI, Inc., model 3080). The aerosol stream was directed into the hydration chamber to equilibrate at different RH. The RH was adjusted by varying the ratio of wet and dry air supplied by a commercial dry air generator (Parker Balston, model 75−62), and the portion of the dry air was sent through water inside a bubbler to generate humidified air. The dry and wet air were then combined in the hydration chamber, and the aerosol particles were directed to a scanning mobility particle sizer (SMPS; TSI, Inc., model 3936) that consisted of a second DMA (DMA2) and a condensation particle counter (CPC; TSI, Inc., model 3025A), where the size distribution of the aerosol population was measured. The RH in the SMPS system was supplied through a Nafion system to the DMA2 sheath air, in which the RH was controlled to nearly equal to that of the RH of the hydration chamber. The RH in the DMA2 was monitored at the DMA inlets of sample and sheath air and at the outlet of the sheath air to ensure the uniformity of the RH in the DMA2. The particle diameters were calculated using a Gaussian function to fit the size distribution.

Bulk Solution Surface Tension Measurements. The bulk surface tension measurements of solutions were performed using Kibron AquaPi force tensiometer (Kibron, Finland) using the Du Noüy-Padday method. The measurements have been previously described in detail by Morris et al., and here we summarize the methodology used to generate bulk trend lines that serve as a comparison with our AFM single particle surface tension measurements.[20] For highly concentrated surface tension measurements, the solution was prepared by gently heating in a closed environment to dissolve the solute. The solution was then allowed to slowly cool to room temperature, before probing for surface tension. After collecting five bulk solution surface tension measurements at a particular solute concentration using the force tensiometer, the relationship between surface tension and solute mole percentage was used to describe a linear dependence for surface-inactive electrolyte salts and saccharides, and logarithmic dependence for surface-active dicarboxylic acids (see Supporting Information for details). The HTDMA water uptake data were used to directly relate solute mole percentage to corresponding RH for each chemical system by using literature values for the saturation point and assumptions on the particle density at low RH.[20] The bulk dependence of the surface tension versus concentration, or RH, was then compared with the AFM single particle results.

Single Particle Surface Tension Measurements Using AFM. Molecular force probe 3D AFM (Asylum Research, Santa Barbara, CA) was used for all force spectroscopy and imaging at ambient temperature and pressure. Custom-made humidity cell was attached to the AFM head to perform studies with varying RH.[20] Silicon nitride AFM probes (MikroMasch, model CSC37) with nominal spring constant of 0.35 N/m were used for particle imaging. High aspect ratio, constant diameter Ag_2Ga nanoneedles (NN-HAR-FM60, NaugaNeedles) with a nominal spring constant of 3.0 N/m were used for limited particle imaging and primarily surface tension measurements. Overall AFM approach was described in detail previously, but here we describe few modifications to the original experimental procedure.[20] For the systematic studies, the nanoneedles all had higher quality control from the manufacturer with three necessary requirements: (1) the offset angle of the needle relative to the substrate was in the range from 0 to 10°, (2) the

DOI: 10.1021/acs.jpca.7b04041
J. Phys. Chem. A XXXX, XXX, XXX−XXX

cutoff point on the end of the needle had degree variance in range from 0 to 10°, and (3) the diameter of the tip was in the range from 50 to 200 nm. For salts and dicarboxylic acids, the surface tension measurements were performed in hydration mode, where the RH is slowly increased from low to high. In consideration of the high viscosity of the saccharides such as glucose, sucrose, and maltose, the surface tension measurements were performed in dehydration mode, where the RH is initially increased to a maximum value (~97% RH), and then slowly decreased. At least three force plots were collected over an individual particle per RH value, which would produce representative averaged data but also limit the possibility of altering the size and shape of the tip as a result of repeated force measurements. After every RH change, each surface tension measurement included ~10−15 min of waiting period to allow the substrate-deposited particles to come to thermodynamic equilibrium with respect to the water vapor in the humidity cell. By measuring the retention force from a reference standard with known surface tension, and calculating the effective nanoneedle radius, we have ensured that the size of the tip does not change during the surface tension measurements of single particles. Specifically, clean vacuum oil (DirecTorr, CAS No. 64742-65-0) was chosen as the calibration standard due to both high stability of surface tension in room temperature and presence of clean break-off point in our force profile (Figure S1). If the force profile showed drastic changes in the tip radius before or after single particle analysis, then the experiment was stopped and the nanoneedle was replaced. As an additional control, AFM force profiles collected over bulk deionized (DI) water were used to measure the surface tension (Figure S2), yielding the surface tension value that is in agreement with the literature.

RESULTS AND DISCUSSION

The imbalance in the intermolecular forces between the surface molecules versus the bulk contributes to macroscopic behaviors such as the curved interface for liquid droplets and surface tension. Thus, the general equation for surface tension σ is defined as the ratio of force over unit length for bulk solution. Extending this to micro-Wilhelmy plate method applicable for the nanoneedle used in this study, the equation for surface tension is expressed as a ratio of force acting on the nanoneedle and the circumference

$$\sigma = \frac{F_{\text{ret}}}{2\pi r} = \frac{F_{\text{pull-in}}}{2\pi r \cos(\theta_e)} \quad (1)$$

where F_{ret} is the retention force, $F_{\text{pull-in}}$ is the pull-in force, r is radius of the nanoneedle, and θ_e is the equilibrium contact angle between the meniscus and nanoneedle.[20] The radius of the nanoneedle is determined by measuring the retention force over a reference liquid (vacuum oil) and further validated with the value measured by scanning electron microscopy (SEM). To identify other key variables in our force profiles, a model force profile with a schematic is shown in Figure 1, where the force acting on the nanoneedle AFM probe is shown as a function of vertical piezo position. Vertical piezo position refers to the position of the AFM probe in z-direction, which is perpendicular to the substrate. Red line indicates approach, and blue line indicates retract from the substrate. The pull-in force is measured when the probe is abruptly pulled into the bulk of the liquid after contact with the droplet, which occurs at the distance where gradient of interaction forces becomes greater

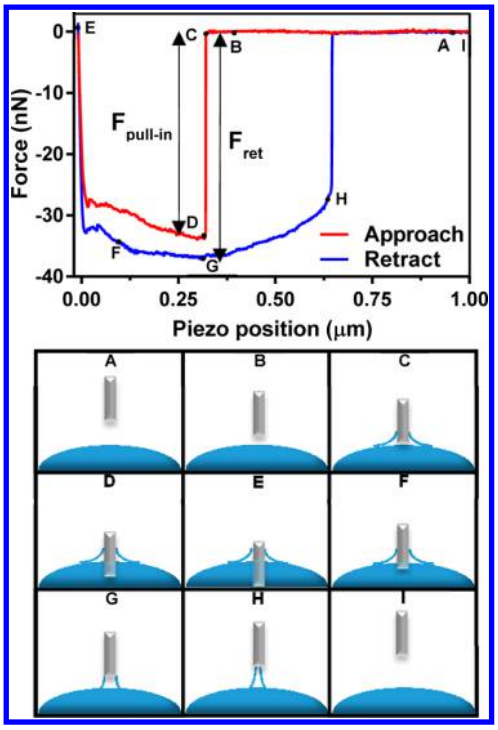

Figure 1. (top) Typical force vs piezo position profile collected over an individual submicron maleic acid particle (at approximate center) showing AFM approach (red line) and retract (blue line) data at 84% RH at various piezo positions indicated in the profile. (bottom) Schematic of contact angles formed from the meniscus to the nanoneedle probe. The relative proportions were exaggerated, and the AFM cantilever is not shown. The silver bar represents the Ag_2Ga nanoneedle grown on the AFM probe. The blue hemisphere represents the surface of particles probed in this study. From the starting position A, the probe approaches down to position B. At position C, the nanoneedle touches the surface, and there is an abrupt formation of the meniscus. Because of this downward pull force, AFM probe pulls down into the bulk of the particle, position D. The probe continues to push through the bulk of the particle until it reaches a predefined loading force, 1 nN in this case, at position E. The piezo reverses direction, and the probe moves away from the surface toward position F. At position G, the retention force is defined as the maximum force recorded that is equivalent to full wetting, or contact angle equal to 0°. Further retracting from the surface thins the meniscus, shown on position H, after which the meniscus breaks and the probe jumps away from the surface. Finally, the probe returns to its original position I, away from the particle.

or equal to the spring constant of the probe. The probe then continues its downward trajectory through the droplet and toward the substrate. After reaching a predefined maximum force, it reverses in vertical direction and retracts away from the surface. The retention force is defined as the maximum force required to break the meniscus off the nanoneedle, which corresponds to the condition where the contact angle θ_e is 0°, that is, complete wetting at position G. Continued motion away from the surface shows decrease in force due to the thinning of the meniscus relative to the probe, after which the meniscus breaks and the probe jumps away from the surface. Finally, the probe returns to its original position I, away from the particle. Therefore, measuring the retention force and using eq 1 allows us to directly quantify surface tension of a droplet at a selected RH.

Single Particle (AFM) and Bulk Solution Surface Tension Measurements. As the particle takes up more

DOI: 10.1021/acs.jpca.7b04041
J. Phys. Chem. A XXXX, XXX, XXX−XXX

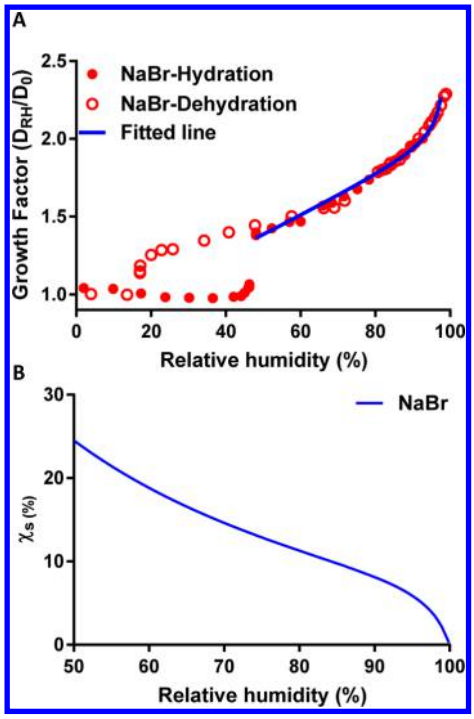

Figure 2. HTDMA growth factor vs RH data for NaBr (A). (red ●) GF data in hydration mode, (red ○) data in dehydration mode. From the hydration curve beyond the deliquescent point at ∼45% RH, eq 2 is used to calculate experimental parameters *a*, *b*, and *c*. From the calculated experimental parameters, a corresponding relationship between solute mole percentage (χ_S) and RH can be expressed using eq 3, shown in blue line (B).

water with increasing RH, it becomes more dilute and decreases the solute concentration, which changes the surface tension. To quantify the relationship between RH and concentration in our AFM experiments, we rely on water uptake measurements of corresponding chemical species. As a representative example of the approach, the HTDMA growth factor data for NaBr is shown (Figure 2A) in both hydration and dehydration modes as red circles and open red circles, respectively. Beyond the deliquescent point at ∼45% RH, the size of the particle continuously increases with RH due to water uptake. Equation 2 was used to fit the growth factor data with *a*, *b*, and *c* as free fit parameters that are specific to the chemical system (Table 1).[25] This allows for direct relationship between RH and GF, which can be used to solve for eq 3, in turn yielding a direct

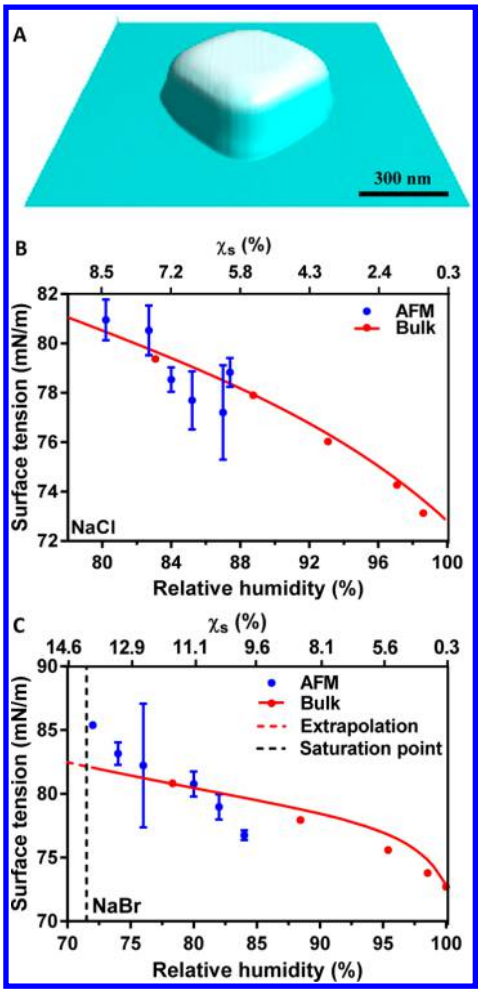

Figure 3. Representative AFM 3D height image at ∼20% RH of NaCl particle with height of ∼350 nm (A). Surface tension vs RH (bottom horizontal axis) and corresponding solute mole percentage (top horizontal axis) for ∼500 nm diameter NaCl (B) and ∼700 nm diameter NaBr (C) individual particles. (blue ● with error bars) Average AFM surface tension data and two standard deviations. (red ●) Bulk solution surface tension measurements. Because of the low standard deviation, the error bars for the bulk data are smaller than the size of the symbol. Red solid line is the bulk trend line that was obtained from eqs 2, 3, and 5. Red dashed line is the extrapolation of the bulk trend line above the saturation point, which is indicated by the vertical black dashed line.

Table 1. Summary of HTDMA Growth Factor Fit Parameters, Bulk Solution Surface Tension Fit Parameters, Dry Solute Densities, Saturation Solute Mole Percentage, and Corresponding RH for Electrolyte Salts, Dicarboxylic Acids, and Saccharides

system	*a*	*b*	*C*	$d\sigma/dC^a$	$\Gamma^{\infty\,b}$	B^c	$\rho_s^{d,f}$	$(\chi_{sat}, RH_{sat})^{e,f}$
NaCl	4.888 14	−3.603 09	−0.315 63	1.71			2.17	(9.99, 75.3)
NaBr	−0.259 72	7.331 83	−6.965 31	1.33			3.20	(13.6, 71.5)
glucose	0.123 50	0.573 06	−0.624 32	1.47			1.54	(10.6, 90.7)
sucrose	0.093 39	0.599 90	−0.644 75	2.27			1.58	(9.65, 85.0)
maltose	0.075 10	0.535 50	−0.580 50	1.73			1.54	(5.16, 96.5)
1glucose/2NaCl	−2.285 58	10.108 80	−7.728 16	1.48			1.91	(9.99, 85.0)
malonic acid	1.599 35	1.538 92	−2.485 41		6.96	0.0208	1.62	(11.3, 71.0)
glutaric acid	0.171 14	0	0		1.81	0.138	1.43	(8.45, 92.7)
maleic acid	0	0.140 82	0.160 47		1.66	0.264	1.59	(10.9, 89.0)

[a]Units (mN m^{-1} M^{-1}). [b]Units (1×10^{-4} mol m^{-2}). [c]Units (M). [d]Units (g/mL). [e]Units (%). [f]Taken from CRC Handbook of Chemistry and Physics.[45]

DOI: 10.1021/acs.jpca.7b04041
J. Phys. Chem. A XXXX, XXX, XXX−XXX

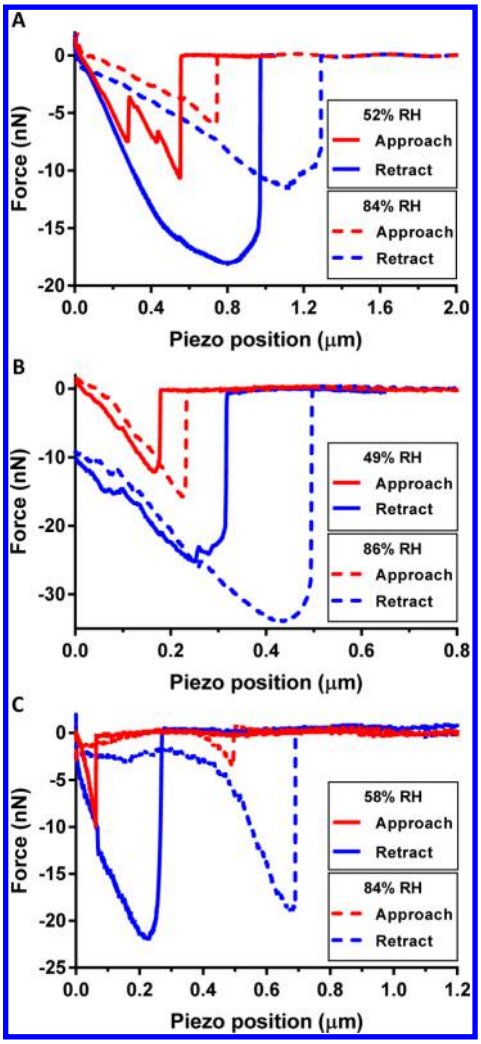

Figure 4. Representative force profiles of electrolyte salt NaBr showing semisolid phase response at 52% RH and liquid behavior at 84% RH (A), dicarboxylic acid malonic acid showing liquid behavior at 49% and 86% RH (B), and saccharide sucrose showing semisolid phase response at 58% RH and liquid behavior at 84% RH (C) are shown. Red line indicates approach and blue line indicates retract at specified RH. Dashed lines represent a force profile of the same single particle, but at a higher RH and subsequently lower solute mole percentage. The maximum applied force was 1 nN for all cases.

relationship between RH and solute mole percentage (Figure 2B) for the specific chemical system:

$$GF^3 = \left[1 + (a \cdot a_w^{\,2} + b \cdot a_w + c)\frac{a_w}{1 - a_w}\right] \quad (2)$$

$$\chi_s(\%) = 100 \cdot \left[1 + \left[\frac{MW_S}{MW_{H_2O}} \cdot \frac{\rho_S}{\rho_{H_2O}} \cdot (GF^3 - 1)\right]\right]^{-1} \quad (3)$$

where $\chi_s(\%)$ is solute mole percentage, MW_S is molecular weight of solute,MW_{H_2O} is molecular weight of water, ρ_S is density of dry solute, ρ_{H_2O} is density of water, GF is growth factor, and a_w is water activity, or RH(%) = 100·a_w. This is crucial analysis to compare our AFM and bulk solution surface tension data, which was performed for all chemical systems reported here. Once the relationship between the GF and RH is established using HTDMA data and fit to eq 2, the bulk surface tension measurements at a specific solute concentration obtained from the force tensiometer can be directly compared with the single particle surface tension measurements at corresponding RH obtained with the AFM. The bulk surface tension is initially measured as a function of solution molarity, which is converted to solute mole percentage and RH by using the growth factor data and the fitted experimental parameters from eqs 2 and 3:

$$GF^3 = \frac{\rho_S}{MW_S} \cdot \frac{1}{C(\text{mol/L})} \quad (4)$$

where C is concentration in molarity. Therefore, with the direct relationship between concentration in molarity to RH and solute mole percentage for bulk surface tension measurements, a bulk surface tension dependence can be related to the growth factor data using the following equations:

$$\sigma(\text{mN/m}) = \sigma_{H_2O} + \frac{d\sigma}{dC} \cdot \frac{\rho_S}{MW_s \cdot GF^3} \quad (5)$$

$$\sigma(\text{mN/m}) = \sigma_{H_2O} - RT\Gamma^{\infty} \ln\left(1 + \frac{\rho_S}{B \cdot MW_S \cdot GF^3}\right) \quad (6)$$

where σ(mN/m) is surface tension at a particular RH or GF, σ_{H_2O} is surface tension of water, $\frac{d\sigma}{dC}$ is change in surface tension as a function of concentration in molarity, R is gas law constant, T is temperature, Γ^{∞} is the maximum surface excess, and B is the inverse Langmuir adsorption constant. Equation 5 is suitable for surface-inactive compounds such as electrolyte salts and saccharides, whereas eq 6 is suitable for surface-active compounds such as dicarboxylic acids.[26,27] Overall, eqs 5 and 6 permit a direct comparison between single particle AFM and bulk solution surface tension data that are expressed as surface tension versus RH and solute mole percentage (see Supporting Information for all derivations). Figures S3 and S4 show HTDMA growth factor data and corresponding solute mole percentage determined using the approach described above as a function of RH for dicarboxylic acids, saccharides, and glucose/NaCl 1:2 mass ratio mixture.

Electrolyte Salts AFM Results. Figure 3 shows single particle AFM surface tension data (blue ●) on single-component electrolyte salt systems (NaCl and NaBr), compared with the bulk surface tension measurements (red ●) at the relevant RH and solute mole percentage ranges. The bulk trend line (red solid line) is obtained using eq 5 as discussed above and extrapolated above the saturation point (red dashed line). We also identified the saturation point in our data (black dashed line) and reported corresponding RH or solute mole percentage for all systems studied here in Table 1. As NaCl is one of the most abundant electrolyte salts present in SSA, it was chosen as the first model system.[2,8,28] A representative three-dimensional (3D) AFM height image of solid NaCl particle at ∼20% RH is shown (Figure 3A); NaBr has similar prism-shape crystalline morphology. AFM surface tension data of NaCl were taken from Morris et al.; however, the range of RH probed was limited from 80% to 87% RH (Figure 3B) due to high deliquescent point of NaCl at ∼75% RH.[23,29,30] The complete deliquescence of NaCl particle to liquid phase state is confirmed by AFM force profile data collected over the droplet at 83% RH (Figure S5). Within the reported RH and concentration range, we observe excellent

DOI: 10.1021/acs.jpca.7b04041
J. Phys. Chem. A XXXX, XXX, XXX−XXX

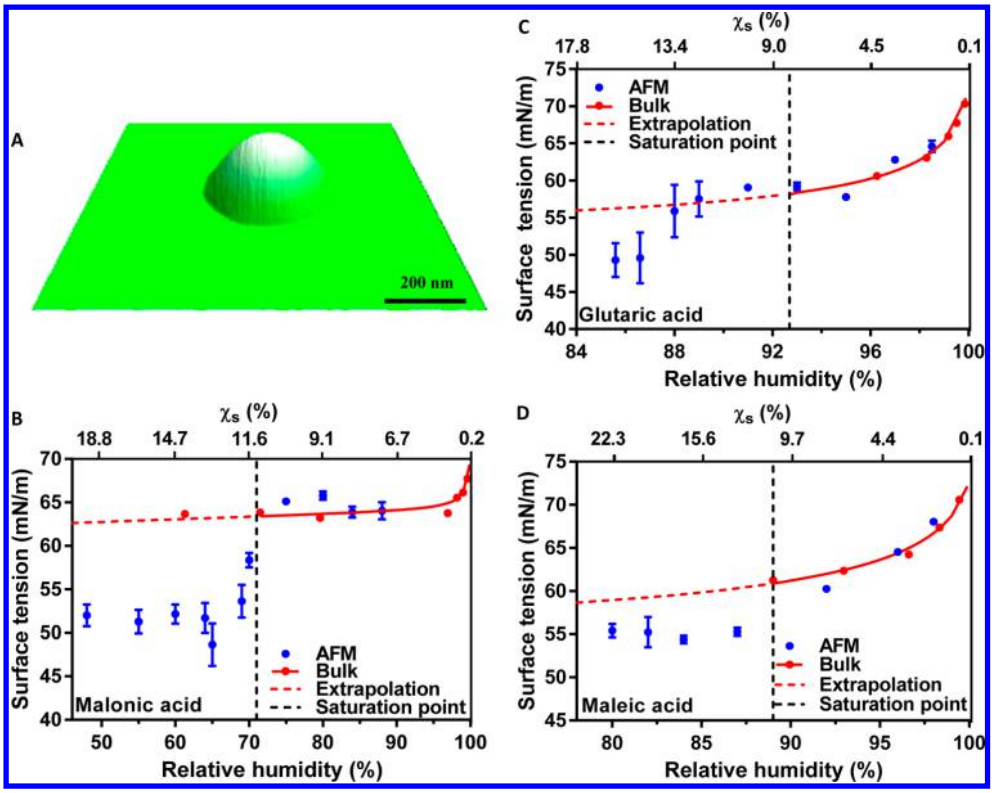

Figure 5. Representative AFM 3D height image at ∼20% RH of glutaric acid particle with height of ∼80 nm (A). Surface tension vs RH (bottom horizontal axis) and corresponding solute mole percentage (top horizontal axis) for ∼800 nm diameter malonic acid (B), ∼ 400 nm diameter glutaric acid (C), and ∼900 nm diameter maleic acid (D) individual particles. (blue ● with error bars) Average AFM surface tension data and two standard deviations. (red ●) Bulk solution surface tension measurements. Because of the low standard deviation, the error bars for the bulk data are smaller than the size of the symbol. Red solid line is the bulk trend line that was obtained from eqs 2, 3, and 6. Red dashed line is the extrapolation of the bulk trend line above the saturation point, which is indicated by the vertical black dashed line.

overlap of AFM single particle surface tension data with bulk surface tension values, which indicates that the new method of comparison between AFM surface tension versus RH and bulk surface tension versus solute mole percentage using HTDMA growth factor data is accurate. We note that this approach provides a superior method than molarity calculations originally reported in Morris et al., which underestimated the relative volume of the solute compared to the solvent.[20]

NaBr is another important electrolyte salt model system present in SSA, although at a much lower concentration relative to NaCl.[31] Figure 3C shows surface tension data of NaBr as a function of RH or corresponding solute mole percentage. Similar to the NaCl results above, surface tension increases with decrease in RH. Additionally, the surface tension measurements at 72% and higher show good overlap between the AFM measurements and bulk tensiometer measurements at the same relevant solute mole percentage ranges. Force profile data collected over the NaBr droplet at these humidity values show liquid behavior in the contact region of the force profile (Figure 4A), similar to NaCl. However, the force profiles recorded at RH values at 67% and lower (above saturation point) show evidence of semisolid particle phase. To better illustrate appearance of the semisolid particle response, we show in Figure 4A the force profile collected at 52% RH, well above the saturation point. Specifically, in the contact region where piezo positions are lower than the position where the probe is pulled into the bulk of particle, the approach curve at 52% RH is vastly different from that at 84% RH. The rough and jagged profile of the contact region for 52% RH indicates that, under supersaturated conditions, the NaBr is highly viscous, displaying a semisolid particle phase response to external applied force, and provides a considerable amount of resistance against the nanoneedle that is indenting through the particle. This is contrary to the smooth force profile in the contact region for 84% RH, which does not show indications of strong resistance against the nanoneedle that is indenting through the liquid droplet. Therefore, once force profiles start to show evidence of the semisolid particle phase state behavior, the measured retention force can no longer be solely attributed to the capillary forces responsible for surface tension but now have additional contributions that include viscosity. Currently, it is not possible to unambiguously decouple the contributing factors; herein, we only report single particle AFM surface tension data at the range of RH where force profiles show liquid-phase behavior in the contact region; thus, the retention force can be assumed to be solely attributed to the surface tension as described by eq 1. In the case of NaBr, force profiles recorded at RH values below 70% started to show evidence of semisolid particle phase response; hence, only force measurements for RH > 70% are shown in Figure 3C.

Dicarboxylic Acids and Saccharides Single Particle AFM Results. In Figures 5 and 6, the AFM surface tension data on single-component organic systems containing dicarboxylic acids and saccharides are shown, respectively. The dicarboxylic acids were chosen due to their abundance in SSA as well as fundamental importance in their tendency to be surface-active, although less than monocarboxylic acids.[21,26,27,32−34] In general, surface-active chemical species

DOI: 10.1021/acs.jpca.7b04041
J. Phys. Chem. A XXXX, XXX, XXX−XXX

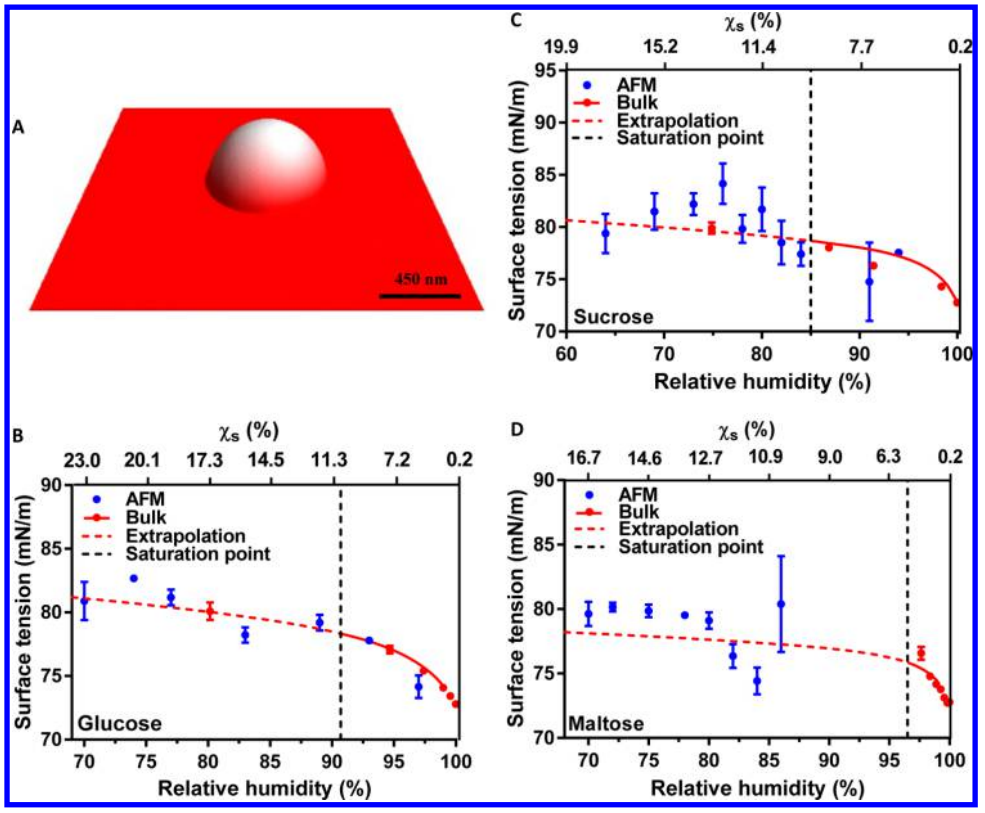

Figure 6. Representative AFM 3D height image at ∼20% RH of glucose particle with height of ∼350 nm (A). Surface tension vs RH (bottom axis) and corresponding solute mole percentage (top horizontal axis) for ∼800 nm diameter glucose (B), ∼600 nm diameter sucrose (C), and ∼1 μm diameter maltose (D) individual particles. (blue ● with error bars) Average AFM surface tension data and two standard deviations. (red ●) Bulk solution surface tension measurements. Because of the low standard deviation, the error bars for the bulk data are smaller than the size of the symbol. Red solid line is the bulk trend line that was obtained from eqs 2, 3, and 5. Red dashed line is the extrapolation of the bulk trend line above the saturation point, which is indicated by the vertical black dashed line.

lower the bulk surface tension values and display an opposite trend to electrolyte salts seen in Figure 3. This is due to the preferential molecular partitioning up to the air−droplet interface. In Figure 5, we show surface tension results for three dicarboxylic acids, malonic acid (MA), glutaric acid (GA), and maleic acid (MeA), that all have similar trends in decreasing surface tension with decreasing RH. As a representative example, 3D AFM height image of GA particle at ∼20% RH is shown (Figure 5A); other acids have similar rounded amorphous morphology. Following the same approach to salts above, water uptake HTDMA data of individual chemical species are used to calculate the solute mole percentage from corresponding RH. The line through the bulk data and the extrapolation of the line to supersaturated concentration conditions was obtained using eq 6 to calculate the predicted surface tension values.[27]

Noteworthy, MA shows good overlap with bulk surface tension data from 75% to 88% RH, but there is a strong negative deviation below 75% RH (Figure 5B). Above the saturation point, the surface tension is lower than the extrapolated prediction from bulk, and below 70% RH, it starts to plateau at ∼52 mN/m. We believe that this behavior may originate from the meniscus formation, where MA molecules form a closely packed molecular film at and below 70% RH at the liquid droplet−air interface on the solid nanoneedle surface. Moreover, the following plateau may be due to the formation of multilayers in the meniscus.[12] After packing the meniscus liquid−air interface, the rest of the molecules could partition toward the bulk of the particle, which does not change the surface tension as RH continues to decrease. In fact, Ruehl et al. have previously shown that their two-dimensional (2D) van der Waals equation of state model predicts the minimum surface tension of malonic acid to plateau approximately at 51 mN/m, in reasonable agreement with our experimental data.

To understand the possible role of increased viscosity of MA above the saturation point in our surface tension measurements, we compared the force profiles collected in this experiment, similar to the approach discussed above for NaBr. Although the viscosity of MA increases with decreasing RH, we do not observe any drastic changes within the contact region when comparing 49% and 86% RH force profile data (Figure 4B). The qualitative indications of semisolid response that was observed for NaBr at 52% RH (Figure 4A) with the rough and jagged profiles in the contact region is not present for MA. Instead, our force profiles show that the MA is in the liquid phase state within the examined RH range, in stark contrast to the change observed for NaBr at the lower RH. We note that at the solute concentration of 6 M, the viscosity of MA (∼1 mPa s) is approximately a factor of 2 lower than that of NaBr (∼2 mPa s),[35,36] consistent with the observation that MA remains in the liquid phase state within the reported RH range. Therefore, the viscosity contribution to the measured retention force above saturation point is assumed negligible in comparison to the increased surface activity of the molecules, which seems to dominate the surface tension.

GA surface tension data is shown in Figure 5C and displays behavior similar to MA. There is an excellent overlap between

DOI: 10.1021/acs.jpca.7b04041
J. Phys. Chem. A XXXX, XXX, XXX−XXX

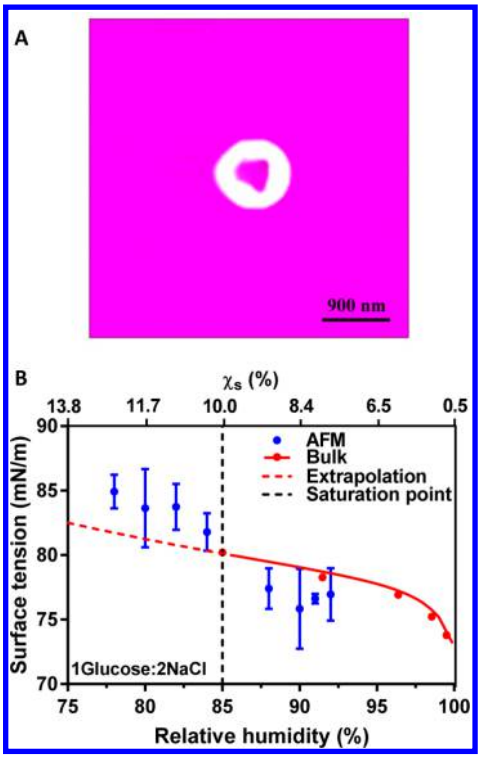

Figure 7. AFM phase image of 1glucose/2NaCl (mass ratio) particle prior to deliquescence at ~50% RH (A). The image shows distinct core−shell morphology, where the pink core is NaCl and the white shell is the glucose coating. Surface tension vs RH (bottom axis) and corresponding solute mole percentage (top horizontal axis) for ~1 μm diameter 1glucose/2NaCl (B) mixture by mass ratio individual particles. For 1glucose/2NaCl, ideal mixing rule was considered to solve for solute concentration. (blue ● with error bars) Average AFM surface tension data and two standard deviations. (red ●) Bulk solution surface tension measurements. Because of the low standard deviation, the error bars for the bulk data are smaller than the size of the symbol. Red solid line is the bulk trend line that was obtained from eqs 2, 3, and 5. Red dashed line is the extrapolation of the bulk trend line above the saturation point, which is indicated by the vertical black dashed line. For the saturation point of 1glucose/2NaCl, solubility data of the pure NaCl was used.

the AFM surface tension data and extrapolated bulk trend line until 88% RH, but subsequent decrease in RH shows the negative deviation that was also observed in MA, although a definite plateau of surface tension to the minimum value is not as evident. However, we hypothesize that further decrease in RH may have ultimately shown a minimum surface tension value, close to 30 mN/m as predicted by Ruehl et al. using the compressed film model.[11] The force profiles collected over GA particle above and below the saturation point do not display drastic differences, and evidence of the semisolid phase response in force profiles starts to appear at 78% RH (Figure S6), implying the particle phase remains liquid-like for RH values greater than 80%. Finally, MeA surface tension behavior is also similar to that of MA and GA, with decreasing surface tension as RH is decreased (Figure 5D). MeA AFM surface tension values show good overlap with bulk surface tension values from 92% to 97% RH but show negative deviation from 80% to 90% RH, similar to MA and GA. The force profiles collected over MeA particle above and below the saturation point (Figure S7) confirm the particle phase remains liquid-like within the reported RH range, similar to other dicarboxylic acids. Above the saturation point, the surface tension values are plateauing at ~55 mN/m, similar in response to that for MA shown from 48% to 70% RH. To the best of our knowledge, MeA minimum surface tension predictions were not performed from either the van der Waals or the compressed film models.

To further examine the applicability of the AFM single particle surface tension measurements over highly viscous chemical systems, three saccharides were chosen. In Figure 6, surface-inactive glucose, sucrose, and maltose show drastically different surface tension behavior compared to surface-active dicarboxylic acids. The surface tension dependence is similar to the surface-inactive electrolyte salts, which increase with increase in the solute mole percentage or decrease in RH. However, unlike inorganic salts, saccharides have a steady water uptake mechanism, as observed in HTDMA hygroscopic data from the lack of a sharp deliquescent point (Figure S4).[37] The lack of obvious crystalline structures at dry RH indicate that the saccharides retain some of their water content even in low humidity conditions, allowing us to probe a wide range of RH for these systems and therefore wider range of viscosity.[38] As an example, representative AFM 3D height image of glucose particle at ~20% RH is shown (Figure 6A); other saccharides display similar amorphous rounded morphology. For the purpose of this study, we focused on RH range that would equate to approximately less than or equal to 1×10^2 Pa s in viscosity, and thus saccharides are expected to be a liquid in phase state.[39−42] In fact, force profiles collected at RH values of 68%, 58%, and 67% for glucose, sucrose, and maltose, respectively, showed evidence of semisolid phase behavior (Figures 4C, S8, and S9). The force profiles collected at these RH values show that the nanoneedle is experiencing a much stronger mechanical resistance as it indents through the particle; thus, the viscosity has increased significantly, and particle is showing semisolid response. However, this behavior is not seen until well above the saturation point, as we observe good overlap between the AFM and bulk extrapolated surface tension values above the saturation point but below 1×10^2 Pa s for glucose, sucrose, and maltose (Figures 6B−D). The lowest RH and corresponding highest viscosity values where force profiles for the saccharides still show liquid response are 70% (ca. $1 \times 10^{0.8}$ Pa s), 64% (ca. $1 \times 10^{1.8}$ Pa s), and 70% (ca. $1 \times 10^{1.9}$ Pa s) for glucose, sucrose, and maltose, respectively.

Electrolyte Salt and Saccharide Binary Mixture AFM Results. Finally, we studied a binary mixture of glucose and NaCl (1:2 mass ratio), and AFM phase image of the mixture particle at ca. 50% RH is shown (Figure 7A). The phase imaging reveals that the particle has a core−shell morphology prior to deliquescence. Ideal volume mixing was considered to convert RH to solute mole percentage, where the NaCl likely contributes more to the overall solute mole percentage compared to the glucose.[43,44] Therefore, the saturation point of the mixture is assumed to be same as pure NaCl. Force profiles showed liquid behavior until 72% RH (Figure S10), where particle phase changes to semisolid. Within the humidity range where binary mixture of glucose and NaCl shows liquid phase response, the AFM surface tension measurements overlap reasonably well compared to the bulk (Figure 7B), confirming the applicability of AFM single particle approach to also study binary mixtures.

■ CONCLUSIONS

In summary, AFM was used to *directly* measure the surface tension of individual sub-micrometer SSA particle mimics at

DOI: 10.1021/acs.jpca.7b04041
J. Phys. Chem. A XXXX, XXX, XXX−XXX

ambient temperature and varying RH conditions. The particles studied in this work consisted of both atmospherically relevant and fundamental models of the following: electrolyte salts, dicarboxylic acids, and saccharide systems. Previously, Morris et al. developed the methodology to measure surface tension of sub-micrometer particles, and here we further improved it with introduction of solute mole percentage determination, more accurate nanoneedle calibration methodology, as well as extended number of chemical systems of increasing complexity studied with increased range of RH and viscosity.[20] The AFM single particle surface tension results are shown to overlap well with the bulk surface tension values for all systems studied at viscosity range below 100 Pa s, further validating the applicability and accuracy of the method. From our model systems, experimental RH range between 80 and 85% was shown to be an optimal point of reference in both solute concentration and viscosity that will likely produce liquid-phase response to applied force. Therefore, applying this methodology to measure the surface tension of more complex single particles of unknown composition while maintaining at least 80% RH should ensure that measured retention force can be solely attributed to surface tension. Toward this end, we are currently extending our *direct* surface tension measurements to more complex systems including lipopolysaccharide (LPS), exopolymeric substances (EPS), and nascent SSA particles that will be published elsewhere. We anticipate that these systems, as well as their mixtures, represent further complexity that can also affect the physicochemical properties and thus surface tension of SSA.

■ ASSOCIATED CONTENT

Supporting Information

The Supporting Information is available free of charge on the ACS Publications website at DOI: 10.1021/acs.jpca.7b04041.

AFM nanoneedle calibration data, HTMDA water uptake results, representative AFM force profiles of individual particles at selected RH, and derivations of relevant equations (PDF)

■ AUTHOR INFORMATION

Corresponding Authors

*Phone: (319)-384-3692. Fax (319)-335-1270. E-mail: alexei-tivanski@uiowa.edu. (A.V.T.)

*Phone: (858)-534-2499. Fax (858)-534-6255. E-mail: vhgrassian@ucsd.edu. (V.H.G.)

ORCID

Armando D. Estillore: 0000-0003-3928-3127

Vicki H. Grassian: 0000-0001-5052-0045

Alexei V. Tivanski: 0000-0002-1528-2421

Present Address

#Center for Free-Electron Laser Science, Deutsches Elektronen-Synchrotron DESY, Notkestrasse 85, 22607 Hamburg, Germany.

Author Contributions

The manuscript was written through contributions of all authors. All authors have given approval to the final version of the manuscript.

Notes

The authors declare no competing financial interest.

■ ACKNOWLEDGMENTS

This work was funded by the National Science Foundation through the Center for Aerosol Impacts on Chemistry of the Environment under Grant No. CHE 1305427. Any opinions, findings, and conclusions or recommendations expressed in this material are those of the authors and do not necessarily reflect the views of the National Science Foundation. We would like to thank Professor Christopher Cappa and Sara Forestieri for helpful discussions.

■ REFERENCES

(1) Prather, K. A.; Bertram, T. H.; Grassian, V. H.; Deane, G. B.; Stokes, M. D.; DeMott, P. J.; Aluwihare, L. I.; Palenik, B. P.; Azam, F.; Seinfeld, J. H.; Moffet, R. C.; Molina, M. J.; Cappa, C. D.; Geiger, F. M.; Roberts, G. C.; Russell, L. M.; Ault, A. P.; Baltrusaitis, J.; Collins, D. B.; Corrigan, C. E.; Cuadra-Rodriguez, L. A.; Ebben, C. J.; Forestieri, S. D.; Guasco, T. L.; Hersey, S. P.; Kim, M. J.; Lambert, W. F.; Modini, R. L.; Mui, W.; Pedler, B. E.; Ruppel, M. J.; Ryder, O. S.; Schoepp, N. G.; Sullivan, R. C.; Zhao, D. F. Bringing the ocean into the laboratory to probe the chemical complexity of sea spray aerosol. *Proc. Natl. Acad. Sci. U. S. A.* **2013**, *110* (19), 7550−7555.

(2) Vignati, E.; Facchini, M. C.; Rinaldi, M.; Scannell, C.; Ceburnis, D.; Sciare, J.; Kanakidou, M.; Myriokefalitakis, S.; Dentener, F.; O'Dowd, C. D. Global scale emission and distribution of sea-spray aerosol: Sea-salt and organic enrichment. *Atmos. Environ.* **2010**, *44* (5), 670−677.

(3) Carslaw, K. S.; Lee, L. A.; Reddington, C. L.; Pringle, K. J.; Rap, A.; Forster, P. M.; Mann, G. W.; Spracklen, D. V.; Woodhouse, M. T.; Regayre, L. A.; Pierce, J. R. Large contribution of natural aerosols to uncertainty in indirect forcing. *Nature* **2013**, *503* (7474), 67.

(4) Pilinis, C.; Pandis, S. N.; Seinfeld, J. H. Sensitivity of Direct Climate Forcing by Atmospheric Aerosols to Aerosol-Size and Composition. *J. Geophys. Res.* **1995**, *100* (D9), 18739−18754.

(5) Cochran, R. E.; Laskina, O.; Trueblood, J. V.; Estillore, A. D.; Morris, H. S.; Jayarathne, T.; Sultana, C. M.; Lee, C.; Lin, P.; Laskin, J.; Laskin, A.; Dowling, J. A.; Qin, Z.; Cappa, C. D.; Bertram, T. H.; Tivanski, A. V.; Stone, E. A.; Prather, K. A.; Grassian, V. H. Molecular Diversity of Sea Spray Aerosol Particles: Impact of Ocean Biology on Particle Composition and Hygroscopicity. *Chem.* **2017**, *2* (5), 655−667.

(6) Haywood, J.; Boucher, O. Estimates of the direct and indirect radiative forcing due to tropospheric aerosols: A review. *Rev. Geophys.* **2000**, *38* (4), 513−543.

(7) Fuentes, E.; Coe, H.; Green, D.; de Leeuw, G.; McFiggans, G. Laboratory-generated primary marine aerosol via bubble-bursting and atomization. *Atmos. Meas. Tech.* **2010**, *3* (1), 141−162.

(8) Jacobson, M. Z. Global direct radiative forcing due to multicomponent anthropogenic and natural aerosols. *J. Geophys Res-Atmos* **2001**, *106* (D2), 1551−1568.

(9) de Leeuw, G.; Andreas, E. L.; Anguelova, M. D.; Fairall, C. W.; Lewis, E. R.; O'Dowd, C.; Schulz, M.; Schwartz, S. E. Production Flux of Sea Spray Aerosol. *Rev. Geophys.* **2011**, *49*.10.1029/2010RG000349

(10) Petters, M. D.; Kreidenweis, S. M. A single parameter representation of hygroscopic growth and cloud condensation nucleus activity. *Atmos. Chem. Phys.* **2007**, *7* (8), 1961−1971.

(11) Ruehl, C. R.; Davies, J. F.; Wilson, K. R. An interfacial mechanism for cloud droplet formation on organic aerosols. *Science* **2016**, *351* (6280), 1447−1450.

(12) Ruehl, C. R.; Wilson, K. R. Surface Organic Mono layers Control the Hygroscopic Growth of Submicrometer Particles at High Relative Humidity. *J. Phys. Chem. A* **2014**, *118* (22), 3952−3966.

(13) Facchini, M. C.; Mircea, M.; Fuzzi, S.; Charlson, R. J. Cloud albedo enhancement by surface-active organic solutes in growing droplets. *Nature* **1999**, *401* (6750), 257−259.

(14) Bzdek, B. R.; Power, R. M.; Simpson, S. H.; Reid, J. P.; Royall, C. P. Precise, contactless measurements of the surface tension of picolitre aerosol droplets. *Chemical Science* **2016**, *7* (1), 274−285.

DOI: 10.1021/acs.jpca.7b04041
J. Phys. Chem. A XXXX, XXX, XXX−XXX

(15) Fitzgerald, J. W. Marine Aerosols - a Review. *Atmos. Environ., Part A* **1991**, *25* (3−4), 533−545.
(16) King, S. M.; Butcher, A. C.; Rosenoern, T.; Coz, E.; Lieke, K. I.; de Leeuw, G.; Nilsson, E. D.; Bilde, M. Investigating Primary Marine Aerosol Properties: CCN Activity of Sea Salt and Mixed Inorganic-Organic Particles. *Environ. Sci. Technol.* **2012**, *46* (19), 10405−10412.
(17) O'Dowd, C. D.; Facchini, M. C.; Cavalli, F.; Ceburnis, D.; Mircea, M.; Decesari, S.; Fuzzi, S.; Yoon, Y. J.; Putaud, J. P. Biogenically driven organic contribution to marine aerosol. *Nature* **2004**, *431* (7009), 676−680.
(18) Cavalli, F.; Facchini, M. C.; Decesari, S.; Mircea, M.; Emblico, L.; Fuzzi, S.; Ceburnis, D.; Yoon, Y. J.; O'Dowd, C. D.; Putaud, J. P.; Dell'Acqua, A. Advances in characterization of size-resolved organic matter in marine aerosol over the North Atlantic. *J. Geophys Res-Atmos* **2004**, *109* (D24).
(19) Facchini, M. C.; Rinaldi, M.; Decesari, S.; Carbone, C.; Finessi, E.; Mircea, M.; Fuzzi, S.; Ceburnis, D.; Flanagan, R.; Nilsson, E. D.; de Leeuw, G.; Martino, M.; Woeltjen, J.; O'Dowd, C. D. Primary submicron marine aerosol dominated by insoluble organic colloids and aggregates. *Geophys. Res. Lett.* **2008**, *35* (17).10.1029/2008GL034210
(20) Morris, H.; Grassian, V.; Tivanski, A. Humidity-dependent surface tension measurements of individual inorganic and organic submicrometre liquid particles. *Chemical Science* **2015**, *6* (5), 3242−3247.
(21) Cochran, R. E.; Laskina, O.; Jayarathne, T.; Laskin, A.; Laskin, J.; Lin, P.; Sultana, C.; Lee, C.; Moore, K. A.; Cappa, C. D.; Bertram, T. H.; Prather, K. A.; Grassian, V. H.; Stone, E. A. Analysis of Organic Anionic Surfactants in Fine and Coarse Fractions of Freshly Emitted Sea Spray Aerosol. *Environ. Sci. Technol.* **2016**, *50* (5), 2477−2486.
(22) Drzymala, J.; Lyklema, J. Surface Tension of Aqueous Electrolyte Solutions. *J. Phys. Chem. A* **2012**, *116* (25), 6465−6472.
(23) Morris, H. S.; Estillore, A. D.; Laskina, O.; Grassian, V. H.; Tivanski, A. V. Quantifying the Hygroscopic Growth of Individual Submicrometer Particles with Atomic Force Microscopy. *Anal. Chem.* **2016**, *88* (7), 3647−3654.
(24) Gibson, E. R.; Hudson, P. K.; Grassian, V. H. Physicochemical properties of nitrate aerosols: Implications for the atmosphere. *J. Phys. Chem. A* **2006**, *110* (42), 11785−11799.
(25) Dick, W. D.; Saxena, P.; McMurry, P. H. Estimation of water uptake by organic compounds in submicron aerosols measured during the Southeastern Aerosol and Visibility Study. *J. Geophys Res-Atmos* **2000**, *105* (D1), 1471−1479.
(26) Aumann, E.; Hildemann, L. M.; Tabazadeh, A. Measuring and modeling the composition and temperature-dependence of surface tension for organic solutions. *Atmos. Environ.* **2010**, *44* (3), 329−337.
(27) Lee, J. Y.; Hildemann, L. M. Surface tension of solutions containing dicarboxylic acids with ammonium sulfate, D-glucose, or humic acid. *J. Aerosol Sci.* **2013**, *64*, 94−102.
(28) Nair, P. R.; George, S. K.; Sunilkumar, S. V.; Parameswaran, K.; Jacob, S.; Abraham, A. Chemical composition of aerosols over peninsular India during winter. *Atmos. Environ.* **2006**, *40* (34), 6477−6493.
(29) Asa-Awuku, A.; Sullivan, A. P.; Hennigan, C. J.; Weber, R. J.; Nenes, A. Investigation of molar volume and surfactant characteristics of water-soluble organic compounds in biomass burning aerosol. *Atmos. Chem. Phys.* **2008**, *8* (4), 799−812.
(30) Ghorai, S.; Tivanski, A. V. Hygroscopic Behavior of Individual Submicrometer Particles Studied by X-ray Spectromicroscopy. *Anal. Chem.* **2010**, *82* (22), 9289−9298.
(31) Guzman, M. I.; Athalye, R. R.; Rodriguez, J. M. Concentration Effects and Ion Properties Controlling the Fractionation of Halides during Aerosol Formation. *J. Phys. Chem. A* **2012**, *116* (22), 5428−5435.
(32) Cochran, R. E.; Jayarathne, T.; Stone, E. A.; Grassian, V. H. Selectivity Across the Interface: A Test of Surface Activity in the Composition of Organic-Enriched Aerosols from Bubble Bursting. *J. Phys. Chem. Lett.* **2016**, *7* (9), 1692−1696.
(33) Boyer, H. C.; Dutcher, C. S. Statistical Thermodynamic Model for Surface Tension of Aqueous Organic Acids with Consideration of Partial Dissociation. *J. Phys. Chem. A* **2016**, *120* (25), 4368−4375.
(34) Tuckermann, R. Surface tension of aqueous solutions of water-soluble organic and inorganic compounds. *Atmos. Environ.* **2007**, *41* (29), 6265−6275.
(35) Chmielewska, A.; Bald, A. Viscosimetric studies of aqueous solutions of dicarboxylic acids. *J. Mol. Liq.* **2008**, *137* (1−3), 116−121.
(36) Abdulagatov, I. M.; Azizov, N. D. Experimental study of the effect of temperature, pressure and concentration on the viscosity of aqueous NaBr solutions. *J. Solution Chem.* **2006**, *35* (5), 705−738.
(37) Marshall, F. H.; Miles, R. E. H.; Song, Y. C.; Ohm, P. B.; Power, R. M.; Reid, J. P.; Dutcher, C. S. Diffusion and reactivity in ultraviscous aerosol and the correlation with particle viscosity. *Chemical Science* **2016**, *7* (2), 1298−1308.
(38) Estillore, A. D.; Morris, H. S.; Or, V. W.; Lee, H. D.; Alves, M. R.; Marciano, M. A.; Laskina, O.; Qin, Z.; Tivanski, A. V.; Grassian, V. H. Linking hygroscopicity and the surface microstructure of model inorganic salts, simple and complex carbohydrates, and authentic sea spray aerosol particles. *Phys. Chem. Chem. Phys.* **2017**, *19* (31), 21101−21111.
(39) Song, Y. C.; Haddrell, A. E.; Bzdek, B. R.; Reid, J. P.; Bannan, T.; Topping, D. O.; Percival, C.; Cai, C. Measurements and Predictions of Binary Component Aerosol Particle Viscosity. *J. Phys. Chem. A* **2016**, *120* (41), 8123−8137.
(40) Shiraiwa, M.; Zuend, A.; Bertram, A. K.; Seinfeld, J. H. Gas-particle partitioning of atmospheric aerosols: interplay of physical state, non-ideal mixing and morphology. *Phys. Chem. Chem. Phys.* **2013**, *15* (27), 11441−11453.
(41) Renbaum-Wolff, L.; Grayson, J. W.; Bertram, A. K. Technical Note: New methodology for measuring viscosities in small volumes characteristic of environmental chamber particle samples. *Atmos. Chem. Phys.* **2013**, *13* (2), 791−802.
(42) Baustian, K. J.; Wise, M. E.; Jensen, E. J.; Schill, G. P.; Freedman, M. A.; Tolbert, M. A. State transformations and ice nucleation in amorphous (semi-)solid organic aerosol. *Atmos. Chem. Phys.* **2013**, *13* (11), 5615−5628.
(43) Jing, B.; Tong, S. R.; Liu, Q. F.; Li, K.; Wang, W. G.; Zhang, Y. H.; Ge, M. F. Hygroscopic behavior of multicomponent organic aerosols and their internal mixtures with ammonium sulfate. *Atmos. Chem. Phys.* **2016**, *16* (6), 4101−4118.
(44) Stokes, R. H.; Robinson, R. A. Interactions in Aqueous Nonelectrolyte Solutions.I. Solute-Solvent Equilibria. *J. Phys. Chem.* **1966**, *70* (7), 2126.
(45) Macdonald, F.; Lide, D. R. CRC handbook of chemistry and physics: From paper to web. *Abstr Pap Am. Chem. S* **2003**, *225*, U552.

DOI: 10.1021/acs.jpca.7b04041
J. Phys. Chem. A XXXX, XXX, XXX−XXX